Hindawi
Geofluids
Volume 2020, Article ID 8889663, 21 pages
https://doi.org/10.1155/2020/8889663

Research Article

Overburden Damage Degree-Based Optimization of High-Intensity Mining Parameters and Engineering Practices in China's Western Mining Area

Xiang He,[1,2] Cun Zhang ,[1,2,3] and Penghua Han[1,2]

[1]*Beijing Key Laboratory for Precise Mining of Intergrown Energy and Resources, China University of Mining and Technology, Beijing 100083, China*
[2]*School of Energy & Mining Engineering, China University of Mining and Technology, Beijing 100083, China*
[3]*State Key Laboratory Cultivation Base for Gas Geology and Gas Control, Henan Polytechnic University, Jiaozuo, 454000 Henan, China*

Correspondence should be addressed to Cun Zhang; cumt_zc@163.com

Received 16 June 2020; Revised 15 July 2020; Accepted 28 July 2020; Published 14 August 2020

Academic Editor: Zhengyang Song

China's western mining area is an arid and semiarid area with a fragile ecological environment, and the high-intensity mining activities aggravate ecological damage. Reasonable choice of the mining parameters (i.e., mining height, panel width, and advancing speed) can not only improve the mining efficiency but also weaken the mining-induced deformation and failures of the overburden and surface. The statistical analysis of the relationship between the mining parameters and periodic weighting interval (PWI) proves that mining parameters have significant influence on overburden failure. In this study, the damage constitutive equation was derived, and the overburden damage degree was defined to quantitatively characterize mining-induced stratum damage in a three-dimensional space. FLAC3D numerical models embedded with a damage constitutive equation were built to compare the panel width effect and advancing speed effect between the overburden damage degree and the water-conducted fracture zone (WCFZ). The reasonable range for mining parameters of the panel 12401 was provided based on the fitting function of the overburden damage degree versus mining parameters. The field measurements were carried out on panel 12401 of the Shangwan coal mine, including the advancing speed, PWI, and ground crack development. The results show that, under constant engineering and geological conditions, the damage degree of overburden will be weakened by increasing the advancing speed, reducing the mining height, or shortening the panel width. The overburden damage degree is more accurate than the height of the water-conducted fractured zone. The reasonable mining parameters of the panel 12401 are 8.8 m in mining height, 300 m in panel width, and 13.47 to 20.58 m/d in advancing speed, respectively. The field measurement results of the PWI and ground cracks have verified the validity using the overburden damage degree to determine high-intensity mining parameters.

1. Introduction

Coal is the dominant energy source in China. In 2018, the total consumption was 4.64 billion tons of standard coal, accounting for 59% of the nation's total energy consumption [1]. China's western mining area is an important energy base for the country, which is typically characterized by large reserves, shallow buried coal seams, simple geological structure, excellent coal quality, and fragile ecological environment [2]. Guo et al. [3] defined high-intensity mining as a high-yield and high-efficiency coal mining method in thick coal seams (more than 3.5 m) with large panel width (more than 200 m), fast advancing speed (more than 5 m/d), high output (usually 5–10 million t/y), a small coal seam depth/thickness ratio (less than 100), and severe overburden and surface failures. For example, the mining height of panel 22307 in the Bulianta coal mine is 7.0 m with a panel width of 450 m and an advancing speed of 21.6 m/d. However, high-intensity longwall mining usually results in a drop of the groundwater table [4], death of vegetation [5], desertification

of land [6], and further deterioration of the fragile ecological environment in these arid and semiarid areas [7]. Therefore, it is one of the research hotspots for both ensuring the safety of high-intensity production and reducing surface ecological damage by optimizing mining parameters.

In general, based on the overburden movement and fracture development, an overburden can be divided into, from bottom to top, a caved zone, a fractured zone, and a continuous zone [8–11]. The water-conducted fracture zone (WCFZ) consists of the caved zone and fractured zone and can be considered plasticized [12]. Hence, its height is important for the safety of underground production and the surface ecological environment (Guo et al. 2018; [13–16]). The height of WCFZ depends on the mining method, mining height, advancing speed, panel width, overburden strength, stratum structure, and geological structure [2, 17–20]. The empirical formula method has been widely used to predict the height of WCFZ. Empirical formulas were usually established on a large number of field measurements with consideration of the rock mechanical strength and mining height; however, most of the field data from the eastern mining areas in China [21]. Guo et al. [3] presented a theoretical study to predict the height of the WCFZ based on the rock failure criteria to determine the maximum suspension length and maximum overhanging length during longwall mining. Liu et al. [22] and Hu et al. [23] obtained the empirical formulas of the height of WCFZ and the weights of variables using multivariate regression analysis. Majdi et al. [12] presented five mathematical approaches to estimate the height of a destressed zone and argued that the height of the destressed zone ranged from 6.5 to 24 times the mining height in the short term and from 11.5 to 46.5 times the mining height in the long term. Some scholars believe that the position and structure of the main key stratum are the determinants of the height of WCFZ. Therefore, key stratum theory is also a common method to predict the height of WCFZ [24–27].

The morphology of the WCFZ is also a main factor to characterize the damage of the overburden. The WCFZ is in a saddle shape after critical mining scale (i.e., length and width) which has been verified by numerous studies [21, 28–30]. Qian et al. [31] found O-shaped mining-induced fracture zone after the gob was compacted, which is the main storage place for gas. Lin et al. [32] established a mathematical model to depict the dynamic evolution of mining-induced fracture elliptic parabolic zone considering the mining height and distance from the first sub-key stratum to the coal seam roof. Wang et al. [33] described the spatial shape of mining-induced fracture as an arch shape through physical modeling. Using FLAC3D modeling, Zhang et al. [34] found that the spatial shape of the WCFZ was a "hat" in the conditions with thick alluvium and thin bedrock. Based on equivalent continuum methods, Zhou et al. [35] developed a new 3D numerical model to simulate the arch-shaped induced fractures in the roof.

Current studies on overburden damage mainly focused on the height and morphology of the WCFZ and provided an important reference for engineering design. However, due to severe surface subsidence and ground cracks are inevitably accompanied with high-intensity mining in the western mining area, the height and shape of the WCFZ cannot quantitatively reflect the damage state of the overburden in three-dimensional space. In addition, when the WCFZ exceeds the surface during shallow coal seams mining and the WCFZ is incomplete in the overburden, the current predictive equations and shape models of the WCFZ become poor to describe the overburden damage. Therefore, this study reports a new method to describe overburden damage based on FLAC3D numerical simulations embedded with a damage constitutive equation. Reasonable mining parameters were determined through the method, and its reliability was verified by the field measurements.

2. Relationship between Mining Parameters and PWI

High-intensity mining usually results in enhanced deformation, overburden damage, and environmental impacts than those in general geological and mining conditions. Rock strata above the gob can be assumed to be the beam (or plates) structure. When the subsidence deformation of the rock stratum exceeds the threshold, it will fracture, leading to the upward development of fractures. Based on Equation (1); the subsidence deformation of the rock stratum is negatively correlated with the comprehensive expansion coefficient [31]. The more fragmentized the roof is, the greater the comprehensive expansion coefficient is. Thus, as the caving interval of the basic roof decreases, the comprehensive expansion coefficient of the rock stratum will increase. Then, the upper rock stratum will be more difficult to fracture because of the decrease of its subsidence space, resulting in the height of the water-conducting fracture zone of the overburden to decrease.

$$\Delta S_i = M - H_i\left(k_{pi} - 1\right), \tag{1}$$

where ΔS_i is the subsidence deformation of the ith rock stratum, M is the mining height, H_i is the height difference between the ith rock stratum and the coal seam, and k_{pi} is the comprehensive expansion coefficient below the ith rock stratum.

Periodic weighting intervals (PWI) and the associated mining parameters were collected from 19 longwall faces in the western mining area (Table 1 and Figure 1).

The PWI is related to many factors, such as rock structure, mining parameters of the working face, coal mining methods, and in situ stress. However, the geological conditions of mines differ greatly from each other. Thus, the same mine adjacent working faces were selected as a case to ensure that the geological and coal seam occurrence conditions are as close as possible and that the influence law of mining parameters on rock fracture is analyzed accurately.

(1) Four adjacent working faces of the Huojitu coal mine and Daliuta coal mine were selected as samples. As shown in Figure 1(a), the panel widths of one mine are same and the mining heights are very close. As shown in Figure 1(b), the PWI has a positive linear correlation with the advancing speed. However, due

Table 1: Mining parameters and PWI of the longwall faces in the western mining area.

No.	Coal mine	Panel name	Panel width (m)	Mining height (m)	Advancing speed (m/d)	PWI (m)
1	Huojitu	21305 (a)	257.2	4.3	5	8.5
2		21305 (b)	257.2	4.3	16	9.9
3		21306 (a)	257.2	4.3	5.2	9.1
4		21306 (b)	257.2	4.3	12.4	9.6
6	Daliuta	52304	301	6.8	13.8	18
7		52307	301	6.8	10.8	17.8
8		52303 (a)	301.5	6.8	4	16.9
9		52303 (b)	301.5	6.8	14	18.2
10	Shangwan	12211	210	5.6	15	13.1
11		12204	300	6.0	13	12.3
12		12205	308	6.0	11.7	12
13		12206	318	6.8	10.1	11.2
14		12201	240	5.3	15	20.6
15	Yujialiang	44201	240	3.1	21.6	15
16		44202	301.1	3	18.7	12
17		44205	296.9	3.3	18.7	11.8
18		44207	360	3.5	16.4	10.7
19		44208	400.5	3.6	15.6	9.9

to the different occurrence conditions of the coal seams, the PWI of the Daliuta coal mine is much longer than that of the Huojitu coal mine

(2) Five adjacent working faces of the Shangwan coal mine were selected as samples, which have approximately equal panel widths and advancing speeds (Figure 1(a)). The influence law of the mining height on the PWI of the main roof was analyzed. As illustrated in Figure 1(c), with a negative exponential relationship between the mining height and PWI and the increase of the mining height, the basic roof is prone to fracture

(3) Similarly, five adjacent working faces in the Yujialiang coal mine were selected as samples to analyze the effect of the panel width on the PWI. As illustrated in Figure 1(d), with the panel width increasing from 240 m to 400 m, the PWI of the basic roof is shortened from 15 m to 9.9 m

From the analysis above, under constant engineering geological conditions, the PWI of the basic roof increases as the advancing speed increases, the mining height reduces, or the panel width shortens. In other words, the degree of overburden damage degree will be weakened for one panel by increasing the advancing speed, reducing the mining height, or shortening the panel width.

3. The Study Site

The Bulianta coal mine and the Shangwan coal mine are located at southwest Ordos City, Inner Mongolia Autonomous Region, as shown in Figure 2(a). Coal 1-2 is the main coal seam of the two coal mines, with a thickness of 7.56–10.79 m and a dip angle of 1–5°. The thickness of the overlying strata is 199–271 m, and thickness of the aeolian layer is 0–34 m in the study site. As demonstrated in Figure 2(b), panel 12511 is the second working face in the 5^{th} district of the Bulianta coal mine, and panel 12401 is the first working face in the 4^{th} district of the Shangwan mine. Panel 12511 was exploited with an average mining height of 7.4 m, a panel width of 319.1 m, and a panel length of 3139.3 m. The BLT-1 drillhole is located 75 m in front of the setup entry and 164 m away from the headgate, and the BLT-2 drillhole is located 909 m in front of the setup entry and 47 m away from the headgate. To maximize the recovery rate of coal resources, the panel 12401 was designed with a panel length of 3139.3 m and a full-seam mining height of 8.8 m which has been the largest mining height in China. Since there were no similar engineering geological conditions before, the mining parameters, especially the panel width and advancing speed, are required to be optimized to ensure the safety and efficiency of mine production and minimize the ecological damage caused by coal exploitation.

4. Damage Constitutive Model

4.1. Basic Hypotheses. Rock mass engineering practice and related experiments show that the deformation and strength characteristics of rock mass belong to the category of brittle failure [36, 37]. Thus, the following hypotheses were made: (a) rock mass is composed of two parts: matrix (noncrack part) and damaged body (microcrack part); (b) the matrix is isotropic elastic medium, and elastic deformation does not cause rock mass damage; (c) the damaged body is rigid perfectly plastic body without yield strength; (d) hydrostatic

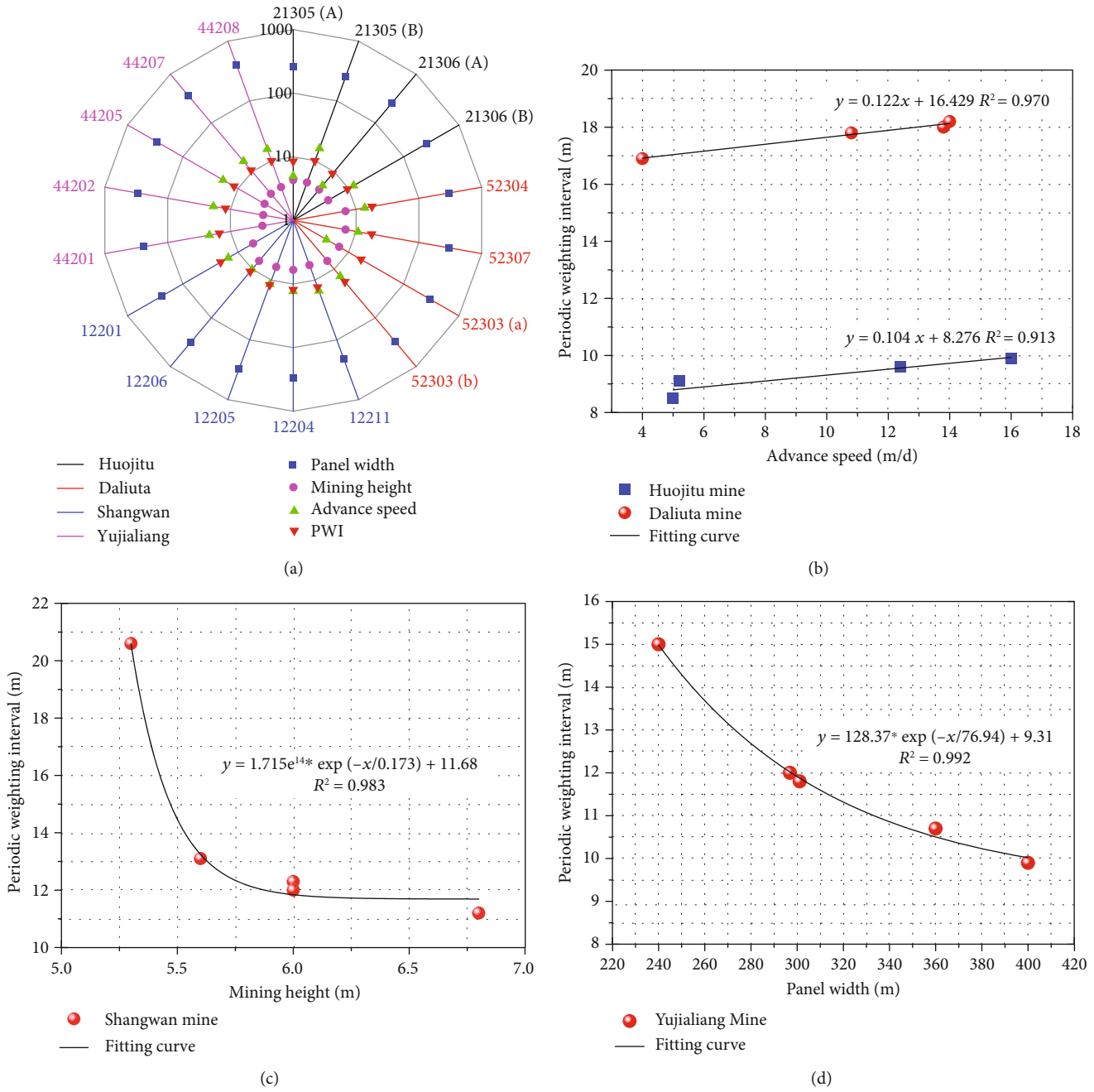

Figure 1: Analysis of the relationship between the mining parameters and PWI. (a) The statistics of the high-intensity mining parameters and the PWI; (b–d) the relationship between the advancing speed, mining height, and panel width, respectively.

pressure does not cause rock mass damage; and (e) the matrix and damaged body conform to the deformation compatibility, that is, the strain is equal. The damage variable of the unit body in the rock mass was defined as follows:

$$D = \frac{dV - dV_0}{dV} = \frac{dV_D}{dV}, \tag{2}$$

where D is the damage variable, dV is the volume of the unit body, dV_0 is the volume of the matrix, and dV_D is the volume of the damaged body, as shown in Figure 3.

4.2. Derivation of Constitutive Equation. The damaged body of rock mass is the stress release zone, and its deviatoric stress is zero. Under the condition of hydrostatic pressure, the cracks in the rock mass tend to close without any damage. Therefore, it can be considered that the damage of the rock mass is mainly caused by the deviatoric stress, and the rock mass stress σ_{ij} and the matrix stress σ_{ij}^0 lie in the identical plane of deviatoric stresses. Thus,

$$J_2 = (1 - D)J_2^0. \tag{3}$$

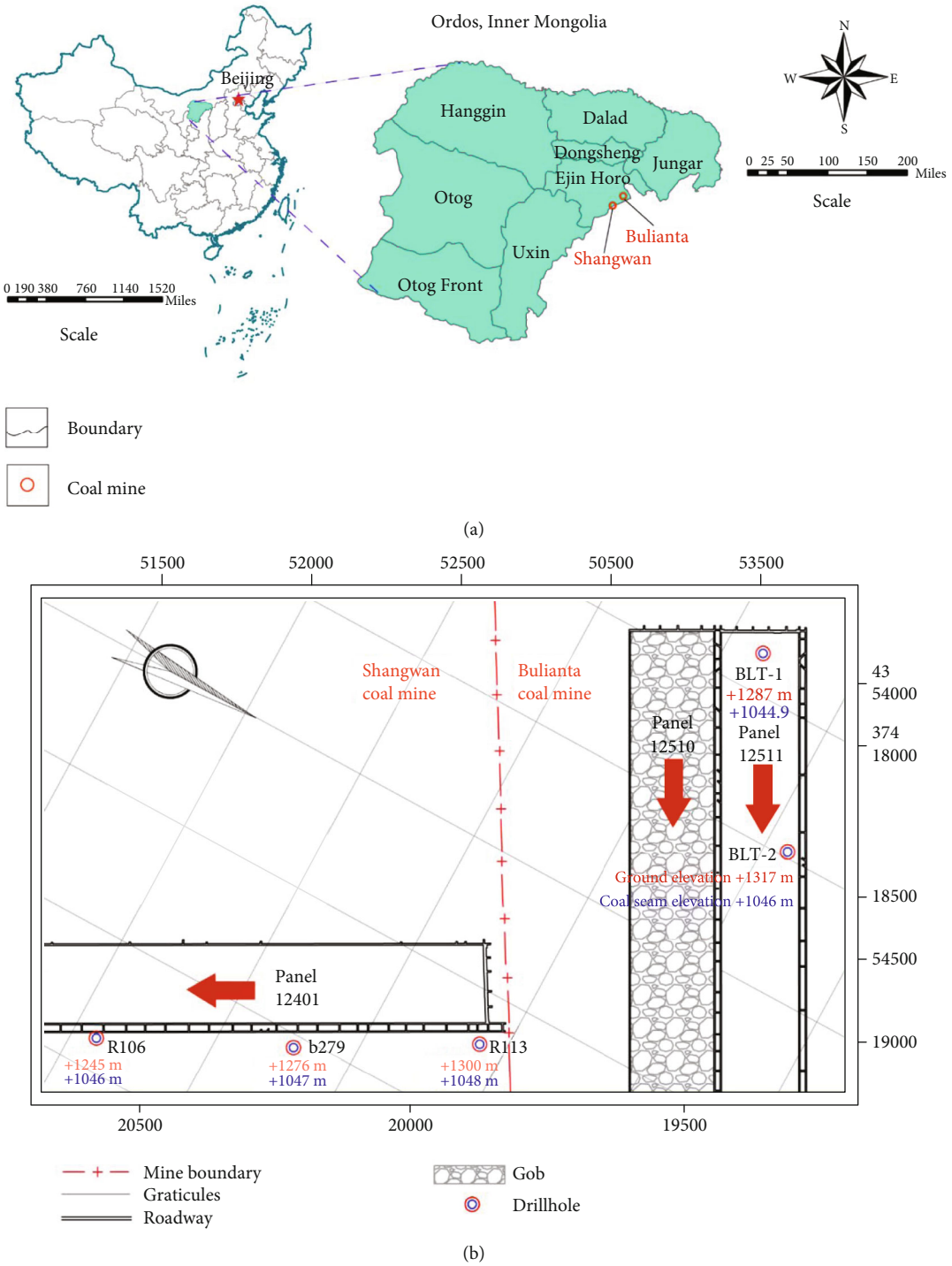

Figure 2: Location of the coal mines (a) and (b) layout of panel 12401 and panel 12511.

Thereinto,

$$J_2 = \frac{1}{2} S_{ij} S_{ji}, \tag{4}$$

$$S_{ij} = \sigma_{ij} - \frac{1}{3} \delta_{ij} \sigma_{mm}, \tag{5}$$

where J_2 and J_2^0 are the second invariants of the deviatoric stress tensor of the rock mass and its matrix, respectively, S_{ij} is the deviatoric stress tensor of the rock mass, σ_{mm} is the hydrostatic pressure, and δ_{ij} is the Kronecker symbol.

Similarly,

$$J_2^0 = \frac{1}{2} S_{ij}^0 S_{ji}^0, \tag{6}$$

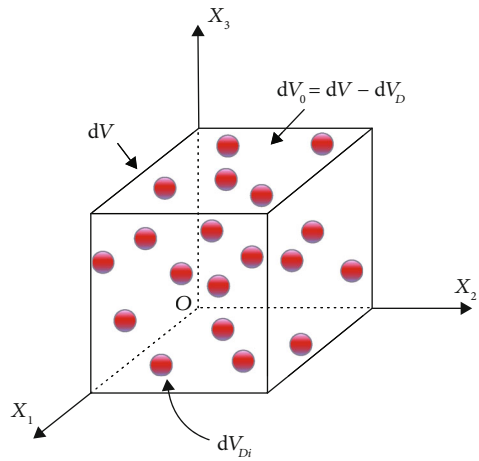

Figure 3: Distribution diagram of the matrix and damaged body in the unit body.

$$S_{ij}^0 = \sigma_{ij}^0 - \frac{1}{3}\delta_{ij}\sigma_m^0. \tag{7}$$

Substituting Equations (4) to (7) into Equation (3),

$$\sigma_{ij} = (1-D)\sigma_{ij}^0 + \frac{1}{3}\delta_{ij}\sigma_{mm} - \frac{1}{3}\delta_{ij}\sigma_{mm}^0 + \frac{D}{3}\delta_{ij}\sigma_{mm}^0. \tag{8}$$

Based on the hypothesis that hydrostatic pressure does not cause damage to the rock mass, that is, $\sigma_{mm} = \sigma_{mm}^0$, Equation (8) can be rewritten as

$$\sigma_{ij} = (1-D)\sigma_{ij}^0 + \frac{D}{3}\delta_{ij}\sigma_{mm}^0. \tag{9}$$

Based on the hypothesis that the matrix is isotropic elastic medium,

$$\sigma_{ij}^0 = E_{ijkl}\varepsilon_{kl}^0, \tag{10}$$

where E_{ijkl} is the elastic constant tensor of the matrix and ε_{kl}^0 is the strain tensor of the matrix.

Based on the hypothesis that the matrix and damaged body conform to the deformation compatibility,

$$\varepsilon_{kl} = \varepsilon_{kl}^0 = \varepsilon_{kl}^D, \tag{11}$$

where ε_{kl}^D is the strain tensor of the damaged body.

Substituting Equations (10) and (11) into Equation (9),

$$\sigma_{ij} = (1-D)E_{ijkl}\varepsilon_{kl} + \frac{D}{3}\delta_{ij}E_{mmkl}\varepsilon_{kl} \tag{12}$$

Equation (12) is the damage constitutive equation of rock mass. However, the volume of the damaged body in rock mass is virtual, which cannot be measured, resulting in Equation (12) is unavailable to practical application. Based on Equations (3) and (11),

$$\begin{aligned} G &= (1-D)G^0, \\ D &= 1 - \frac{G}{G^0}, \end{aligned} \tag{13}$$

where G is the shear modulus of the rock mass and varies with the degree of damage, variable, and G^0 is the shear modulus of the matrix, constant.

The relationship between equivalent stress and equivalent strain in elastoplastic mechanics is as follows:

$$\bar{\sigma} = 3G\bar{\varepsilon}. \tag{14}$$

Based on Equation (14), the change curve of shear modulus G of the rock mass can be obtained by mechanical tests. Substituting Equation (13) into Equation (12),

$$\sigma_{ij} = \frac{G}{G^0}E_{ijkl}\varepsilon_{kl} + \frac{1}{3}\left(1 - \frac{G}{G^0}\right)\delta_{ij}E_{mmkl}\varepsilon_{kl} \tag{15}$$

Equation (15) is the ultimate damage constitutive equation of the rock mass, which is more convenient for practical application than Equation (12).

4.3. Model Verification. During the mining process of panel 12511, the WCFZ was observed using the combination method of washing fluid leakage and drillhole color TV. At the drillhole depth of 24.80–130.71 m, the trend of washing fluid leakage is relatively gentle (Figure 4). Beyond the drilling depth of 130.71 m, the leakage of the washing fluid increased significantly. At 134.74 m, the washing fluid circulation was interrupted, indicating that all the liquid was lost. After the drilling was completed, a drillhole color TV was used for the borehole imaging of the wall. The images obtained showed that the integrity of the strata was good above the drilling depth of 130.2 m, with few original fractures. An inclined fracture with 2 to 3 cm aperture began to appear below the drillhole depth at 130.2 m that was considered to be the top of the WCFZ. The irregular cross fractures began to appear at the drillhole depth of 201.1 m, causing serious damage to the drillhole, which was considered to be the top of the caved zone.

Based on the measured results from the BLT-1, the top of the WCFZ is at a drillhole depth of 130.2 m. The ground elevation of the BLT-1 drillhole is +1287 m, the floor elevation of coal 1–2 is +1044.9 m, and the mining height is 7.1 m. The equation for calculating the height of WCFZ [38] is as follows:

$$H = D - h_f + W, \tag{16}$$

where H_f is the maximum height of WCFZ, H is the mining depth, h_f is the drillhole depth at the top of the WCFZ, and W is the compression value of rock strata in the fractured zone during drilling observation, generally set as $W = 0.2$ M. From the calculation, the measured height of the WCFZ is 106.22 m.

Lithology	Depth (m)	Thickness (m)
Aeolian sand	34.0	34.0
Sandy mudstone	49.0	15.0
Conglomerate	68.6	19.6
Gritstone	100.0	31.4
Conglomerate	109.0	9.0
Mudstone	118.8	9.8
Sandy mudstone	134.1	15.3
Fine sandstone	146.7	12.6
Sandy mudstone	178.2	31.5
Mudstone	187.6	9.4
Sandy mudstone	198.9	11.3
Gritstone	214.9	16.0
Sandy mudstone	235.0	20.1
Coal 1-2	242.1	7.1

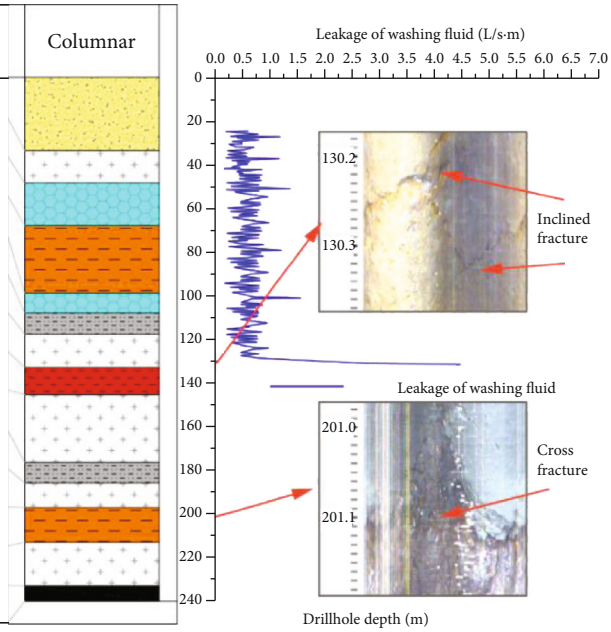

Figure 4: The histogram of the BLT-1 drillhole and the measurement results of WCFZ.

The damage constitutive equation of the rock mass was embedded into the FLAC3D model to simulate the overburden failure. FlAC3D allows operators to use C++ language for custom constitutive model secondary development. The custom constitutive model should be compiled into dynamic Link Library (DLL) and stored in the "exe64\plugins\cModel" folder under the FLAC3D installation directory. After configuration by the "Model Configure Plugin" command, the custom constitutive model can be called. The cycle of FLAC3D is mainly divided into five steps: (1) solving the equilibrium equation according to Newton's second law to get the acceleration of grid node, (2) adopting time integration to calculate node velocity and displacement, (3) the strain rate of the element solved by spatial derivative, (4) updating element stress and state variables based on constitutive model, and (5) calculating the internal forces of grid nodes by element integration. The constitutive model of step (4) in the above steps is realized by secondary development in this paper, and the other steps are automatically calculated by FLAC3D.

The simulation model took the panel of the Bulianta coal mine as the prototype with dimensions of 420 m long × 420 m wide × 267 m high. A fixed boundary, roller boundary, and free boundary were set at the bottom, around, and at the top of the model, respectively. In the numerical simulation models, the excavation area was 50 m from the model boundary to eliminate the boundary effect. The Mohr-Coulomb criterion was adopted in the excavation simulation, and the double-yield constitutive model was applied in the gob elements [39–41]. Based on the lab tests and literature researches, the specific parameters are listed in Tables 2 and 3.

FLAC3D is a finite difference method software, which cannot simulate the height of water-conducting fracture zone. However, the height of plastic zone has been used to indirectly describe the height of water-conducting fracture zone for a long time [42, 43]. After the excavation of the model, the profile of plastic zone was made in the middle of the model, as shown in Figure 5. The shape of WCFZ is similar to saddle shape, and the height of WCFZ is 108.6 m. There is merely a difference of 2.38 m from the measured value of 106.22 m, and the relative error is 2.24%. The simulation result is close to the measured value, indicating that the model embedded with a damage constitutive equation is highly reliable.

5. Optimization of Mining Parameters Based on Overburden Damage Degree

5.1. Definition of the Overburden Damage Degree. With the purpose of overcoming the shortcomings of existing methods for describing overburden damage, the concept of the overburden damage degree was proposed. As shown in Equation (17), the overburden damage degree is defined as the ratio of the total volume of plastic zones to the observation space volume vertically above the excavation range of the coal seam. The greater the overburden damage degree is, the more severe the strata damage is. The overburden damage degree is no longer confined to the spatial form and the three-zone distribution of the overburden and instead quantitatively describes the overburden failure. For numerical simulations, the calculation of the overburden damage degree is relatively convenient and practical.

$$D_d = \frac{\sum_{i=1}^{n} V_i}{V_o} \times 100\%, \tag{17}$$

where D_d is the overburden damage degree, V_i is the volume of a plastic zone, and V_o is the observed space volume.

5.2. Numerical Modeling. In practice, in order to maximize the recovery rate of coal resource, the working face is usually

Table 2: Physical and mechanical parameters of coal and rock mass.

Lithology	Bulk modulus (GPa)	Shear modulus (GPa)	Internal fraction angle (Deg.)	Tensile strength (MPa)	Cohesion (MPa)	Density (kg/m^3)
Aeolian sand	3.3	1.53	36.5	0	3.65*e*-3	1580
Gritstone	6.3	5.5	30	1.78	12.4	2372
Medium sandstone	8.1	6.37	28.1	1.73	18	2484
Fine sandstone	8.4	6.7	22.4	3.57	20.6	2615
Sandy mudstone	3.18	2.40	18	3.77	17.7	2330
Siltstone	3.0	2.47	24.7	2.56	23.1	2295
Mudstone	2.13	0.93	36.6	4.18	11.7	2311
Coal 1-2	1.51	5.7	23.6	1.69	17.9	1280

Table 3: Mechanical parameters of the double-yield gob elements.

Strain	0.0	0.02	0.05	0.07	0.1	0.12	0.15	0.17	0.20
Cap pressure (MPa)	0.0	0.1	0.3	0.6	1.25	2.25	5.0	10.0	20.0

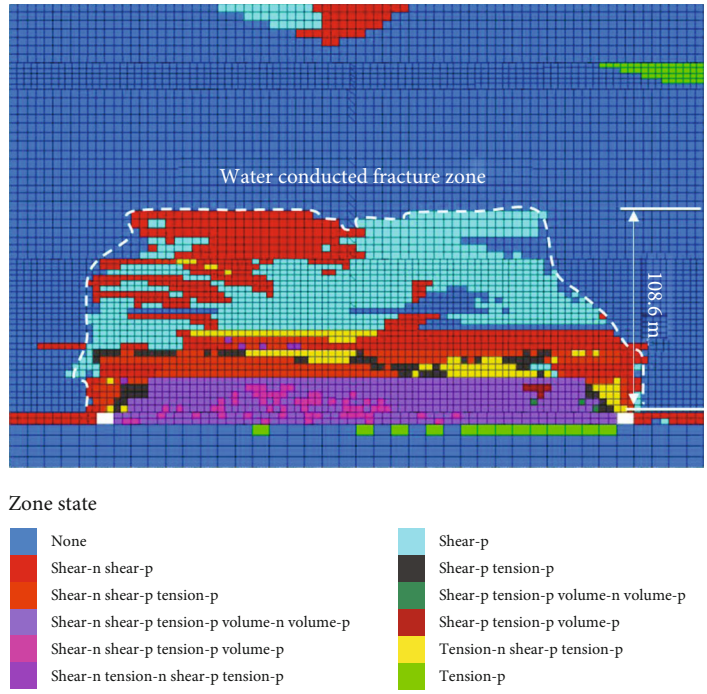

Figure 5: Distribution characteristics of overburden plastic zone in the middle of the model (Y = 200 m plane).

designed with a full-seam mining technology. Thus, the influence of different panel widths and advancing speeds on overburden damage is more significant to production. The FLAC3D numerical models of different panel widths and advancing speeds were established by taking panel 12401 of the Shangwan coal mine as a prototype. As shown in Figure 6, the model height is Z = 235.3 m, and the length is Y = 400 m in the advancing direction, and the model width X is determined by the different panel widths. The settings of the boundary conditions and pillar width of the model were the same as those in Section 4.3. The Mohr-Coulomb criterion was adopted in the excavation simulation, and the double-yield constitutive model was applied in the gob elements. Since panel 12401 is adjacent to the panel 12511 and has the same stratigraphic structure, the selection of physical and mechanical parameters is the same as in Tables 2 and 3.

5.3. Effect of the Panel Width on Overburden Damage. The number of working faces in a mining district will be reduced

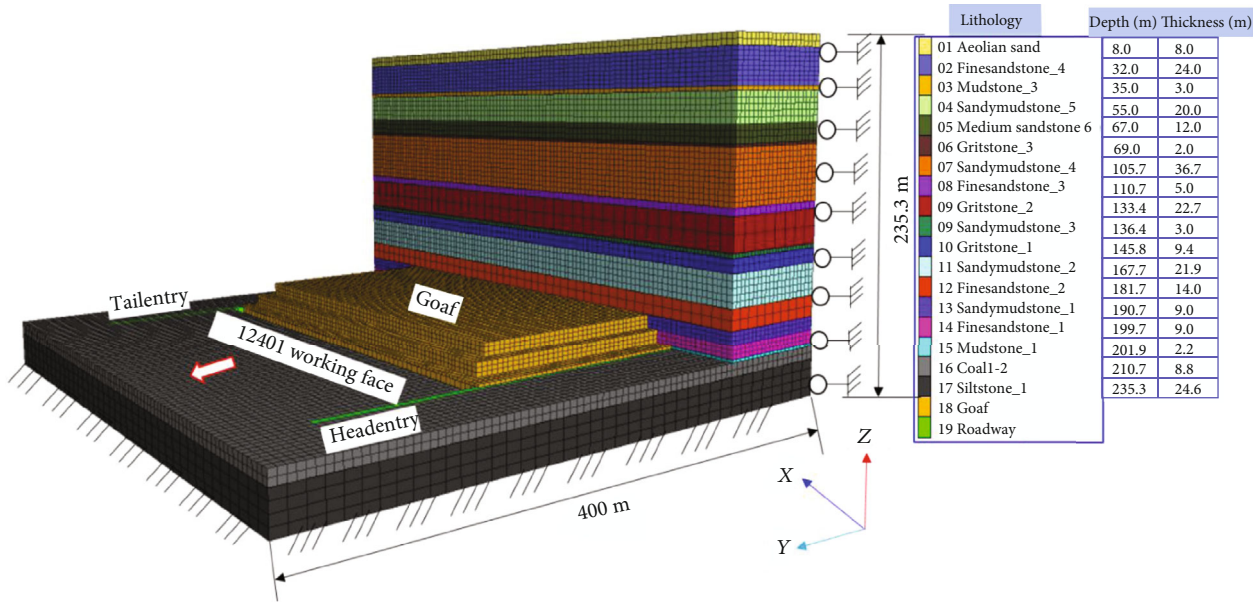

Figure 6: Numerical model of the overburden damage degree.

Table 4: Selection of different panel widths.

Panel width (m)	100	150	200	250	300	350	400	450	500
Model width (m)	200	250	300	350	400	450	500	550	600
Zone number	229478	284356	339100	397278	452156	510300	565178	623356	678100

by increasing the panel width; then, the number of coal pillars will be reduced correspondingly, which is conducive to improving the coal recovery. However, the increase of the panel width leads to a more intensive overburden movement, which is not conducive to the protection of aquifers and surface ecological environment. Nine numerical models with different panel widths (Table 4) were constructed to investigate the influence of the panel width on the overburden damage degree. Base on the current situation of high-intensity mining, the designed panel widths were ranging from 100 to 500 m with a gradient of 50 m. To improve the calculation efficiency, the model width X increased with the panel width on the premise of not affecting the calculation results. The headgate and tailgate were excavated with dimensions 5.0 m wide × 4.5 m high when the initial stress balanced. After the roadways were excavated, the panel 12401 was mined with 8.8 m mining height. The advancing speed was selected as 10 m/d, considering the previous mining experience of the Shangwan coal mine in Section 2.

As shown in Figure 7, cross profiles were made through the center of the models, and the distribution characteristics of the plastic zone with different panel widths were obtained. The plastic zone of the overburden is arch-shaped, and the boundary of the plastic zone is mainly shear failure. As increases in the panel width, the width of the plastic zone increases synchronously and the height of plastic zone increases from 51.72 m to the surface. When the panel width is 250 m, the aeolian sand appears to undergo shear failure, namely, when cracks occur on the surface. When the panel width is 300 m, the height of WCFZ and the depth of the surface failure further increase, but they are not connected. As depicted in Figure 7(e), the height of WCFZ reaches 162.9 m, but the burial depth of the panel 12401 ranges from 124 m to 244 m. Therefore, the coal exploitation of the panel 12401 has potential hazards such as air leakage, water, and sand inrush.

The overburden damage degree of the different panel widths was obtained by writing Fish language. As shown in Figure 8, as the panel width increases, the height of WCFZ and the overburden damage degree increase synchronously, verifying the reliability of the overburden damage degree to describe the overburden failure. The overburden damage degree versus the different panel widths was fitted as follows:

$$y_L = \frac{19.2755 + 72.2692}{1 + e^{-(x-319.8399)/58.0277}}, \quad R^2 = 0.9980. \tag{18}$$

The fitting curve is monotonically increasing, and the inflection point is (319.84, 55.85). Specifically, when the panel width is 319.84 m, the overburden damage degree increases fastest. As illustrated in Figure 6, the overburden of panel 12401 is mainly thick and hard sandstone stratum.

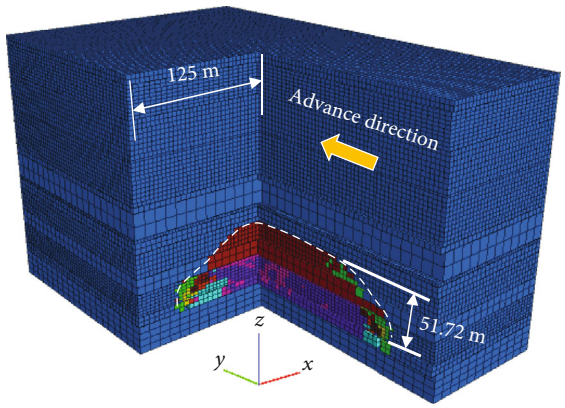

Zone state
- None
- Shear-n
- Shear-n shear-p
- Shear-n shear-p tension-p
- Shear-n shear-p tension-p volume-n volume-p
- Shear-n shear-p tension-p volume-p
- Shear-n tension-n shear-p tension-p
- Shear-n tension-n shear-p tension-p volume-n volume-p
- Shear-n tension-n shear-p tension-p volume-p
- Shear-p
- Shear-p tension-p
- Shear-p tension-p volume-n volume-p
- Shear-p tension-p volume-p
- Tension-n
- Tension-n shear-p
- Tension-n shear-p tension-p
- Tension-n shear-p tension-p volume-p
- Tension-n tension-p
- Tension-p

(a) 150 m

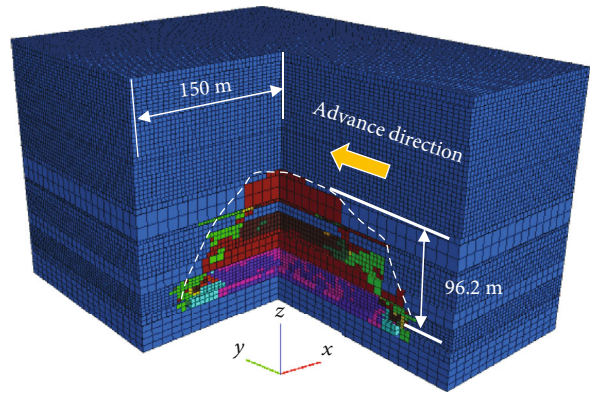

Zone state
- None
- Shear-n
- Shear-n shear-p
- Shear-n shear-p tension-p
- Shear-n shear-p tension-p volume-n volume-p
- Shear-n shear-p tension-p volume-p
- Shear-n tension-n shear-p tension-p
- Shear-n tension-n shear-p tension-p volume-n volume-p
- Shear-n tension-n shear-p tension-p volume-p
- Shear-p
- Shear-p tension-p
- Shear-p tension-p volume-n volume-p
- Shear-p tension-p volume-p
- Tension-n
- Tension-n shear-p
- Tension-n shear-p tension-p
- Tension-n shear-p tension-p volume-p
- Tension-n tension-p
- Tension-p

(b) 200 m

Figure 7: Continued.

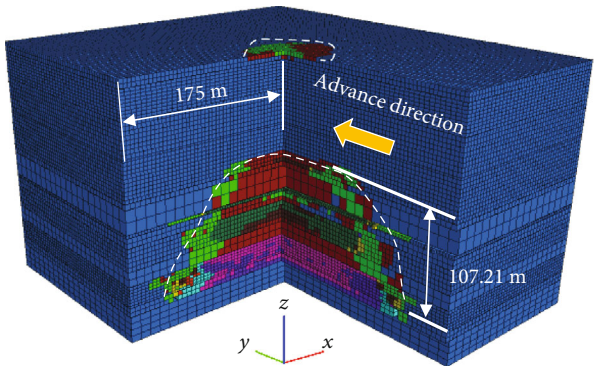

Zone state
- None
- Shear-n
- Shear-n shear-p
- Shear-n shear-p tension-p
- Shear-n shear-p tension-p volume-n volume-p
- Shear-n shear-p tension-p volume-p
- Shear-n tension-n shear-p tension-p
- Shear-n tension-n shear-p tension-p volume-n volume-p
- Shear-n tension-n shear-p tension-p volume-p
- Shear-p
- Shear-p tension-p
- Shear-p tension-p volume-n volume-p
- Shear-p tension-p volume-p
- Tension-n
- Tension-n shear-p
- Tension-n shear-p tension-p
- Tension-n shear-p tension-p volume-p
- Tension-n tension-p
- Tension-p

(c) 250 m

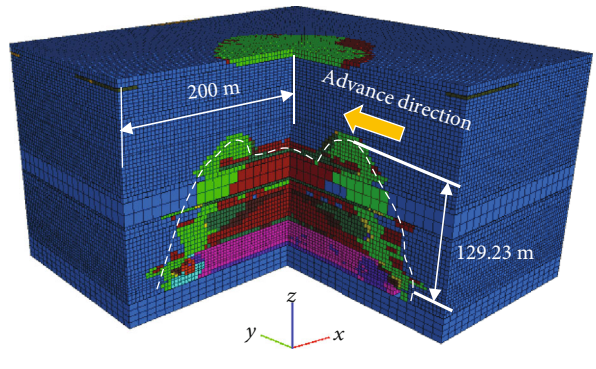

Zone state
- None
- Shear-n
- Shear-n shear-p
- Shear-n shear-p tension-p
- Shear-n shear-p tension-p volume-n volume-p
- Shear-n shear-p tension-p volume-p
- Shear-n tension-n shear-p tension-p
- Shear-n tension-n shear-p tension-p volume-n volume-p
- Shear-n tension-n shear-p tension-p volume-p
- Shear-p
- Shear-p tension-p
- Shear-p tension-p volume-n volume-p
- Shear-p tension-p volume-p
- Tension-n
- Tension-n shear-p
- Tension-n shear-p tension-p
- Tension-n shear-p tension-p volume-p
- Tension-n tension-p
- Tension-p

(d) 300 m

Figure 7: Continued.

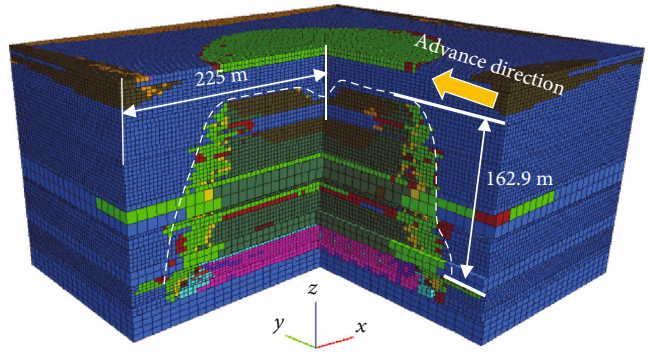

(e) 350 m

Figure 7: Distribution characteristics of plastic zone of the overburden with different panel widths.

The thick and hard strata not only bear the weight of the overlying strata, but also hinder the upward development of fractures below [27, 44]. As the panel width increases from 300 m to 350 m, the overburden damage degree and the height of WCFZ have relatively large increase. The result indicates that the thick and hard strata are broken, which hinder the upward development of fractures. Combined with Figures 6, 7(d) and 7(e), we concluded that the thick and hard stratum mentioned above were the medium sandstone, and the inflection point of the fitting curve was the critical point of the stratum break. Therefore, under the engineering geological conditions of panel 12401 of the Shangwan coal mine, the maximum panel width determined by the overburden damage degree should be less than 319.84 m, which promotes safe and efficient mining. Meanwhile, the panel width is restricted by the available coal mining technology and mechanical equipment. Yi [45] investigated that the reasonable panel width of the Shangwan coal mine determined by the working resistance of hydraulic support should not exceed 300 m.

5.4. Effect of Advancing Speed on Overburden Damage. The tensile strength of the overburden will be improved by speeding up the panel advancing [46]. Nine Numerical models with different advancing speeds were constructed to investigate the influence law of advancing speed on the overburden damage degree. Based on the current situation of high-intensity mining, the designed advancing speed range was 5 to 21 m/d with a gradient of 2 m/d. The dimensions of the models were 400 m wide × 400 m long × 235.3 m high. The headgate and tailgate were excavated with dimensions 5.0 m wide × 4.5 m high when the initial stress balanced. After the roadways were excavated, panel 12401 was mined with 8.8 m mining height and 300 m panel width. Different advancing speeds were simulated through stepwise excavation. The excavated step was equal to the advancing speed value, and the calculation time was 500 steps.

As shown in Figure 9, cross profiles were made through the center of models, and the distribution characteristics of the plastic zone with different advancing speeds were obtained. The plastic zone of the overburden is not connected with the surface, which indicates that the mining height and panel width are reasonably selected. As the advancing speed increases from 5 to 19 m/d, the height of WCFZ decreases from 132.7 to 114.35 m and the dimension of the surface

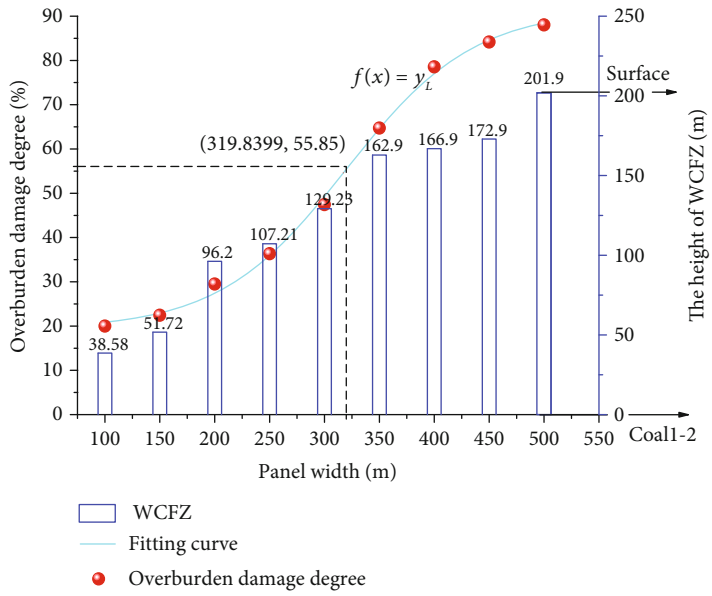

Figure 8: Overburden damage degree and the height of WCFZ versus panel width.

plastic zone decreases in the advancing direction of the working face. The results above indicate that the mining-induced failure on the overburden and surface is weakened as the advancing speed increases.

As shown in Figure 10, both the overburden damage degree and the height of WCFZ show a decreasing trend as the advancing speed increasing. When the advancing speed is 5 to 13 m/d, the height of WCFZ remains at 132.7 m, but different advancing speeds correspond to different overburden damage degree values, thereby indicating that the overburden damage degree is more accurate than the height of WCFZ in describing the overburden damage. The variation range of the overburden damage degree influenced by the advancing speed and panel width is 41% to 49.37% and 19.98% to 88.02%, respectively. Therefore, the damage degree is more sensitive to the variation in panel width. The damage degree with different advancing speeds was fitted as follows:

$$y_v = \frac{0.4105 + 0.0818}{1 + e^{-(x-13.4662)/-1.3243}}, \quad R^2 = 0.9677. \tag{19}$$

The fitting curve is monotonically decreasing, and the inflection point is (13.47, 45.08). Specifically, when the advancing speed is 13.47 m/d, the overburden damage degree decreases fastest. The overburden damage degree and the height of WCFZ change slightly after the inflection point; thus, the reasonable advancing speed of panel 12401 should not be less than 13.47 m/d.

Due to the limited speed of the shearer, the advancing speed of the working face has to simultaneously meet the following equation:

$$v \le \frac{tv'd}{L}, \tag{20}$$

where v is the advancing speed of the working face, t is the cutting time of the shearer, v' is the cutting speed of the shearer, d is the cutting depth, and L is the panel width.

Based on the operation regulations of panel 12401, the shearer cuts coal for 17 hours a day with a running speed of 7 m/min and a cutting depth of 0.865 m. The maximum advancing speed of the working face under ideal conditions is 20.58 m/d through Equation (20). Therefore, the reasonable advancing speed of the working face is 13.47 to 20.58 m/d.

6. Field Practice

Based on the analysis above in this study, the mining parameters of panel 12401 of the Shangwan coal mine were designed as 8.8 m in mining height, 300 m in panel width, and 13.47 to 20.58 m/d in advancing speed. There were no air leakages, water inrushes, surface river interruptions, or other hazards during the entire mining process, indicating that the mining parameters determined by the overburden damage degree were valid.

6.1. Effects of the Advancing Speed on the Periodic Weighting. In the real-world production process, the advancing speed is easier to control than the mining height and panel width without affecting recovery rate of coal resources. During the new equipment debugging period from March 25, 2018, to May 27, 2018 (stage I), mining equipment failed frequently, and the continuity of the coal seam excavation was poor. As shown in Figure 11, the advancing distance of panel 12401 was 246.35 m in stage I, and the distribution of the advancing speed was discrete. The average advancing speed was merely 3.91 m/d, which was much less than the critical advancing speed of 13.47 m/d. During the normal mining period from May 28, 2018, to June 5, 2018 (stage II), the advancing distance reached 369.6 m, and the advancing speed was maintained at the critical value with an average advancing speed of 13.69 m/d.

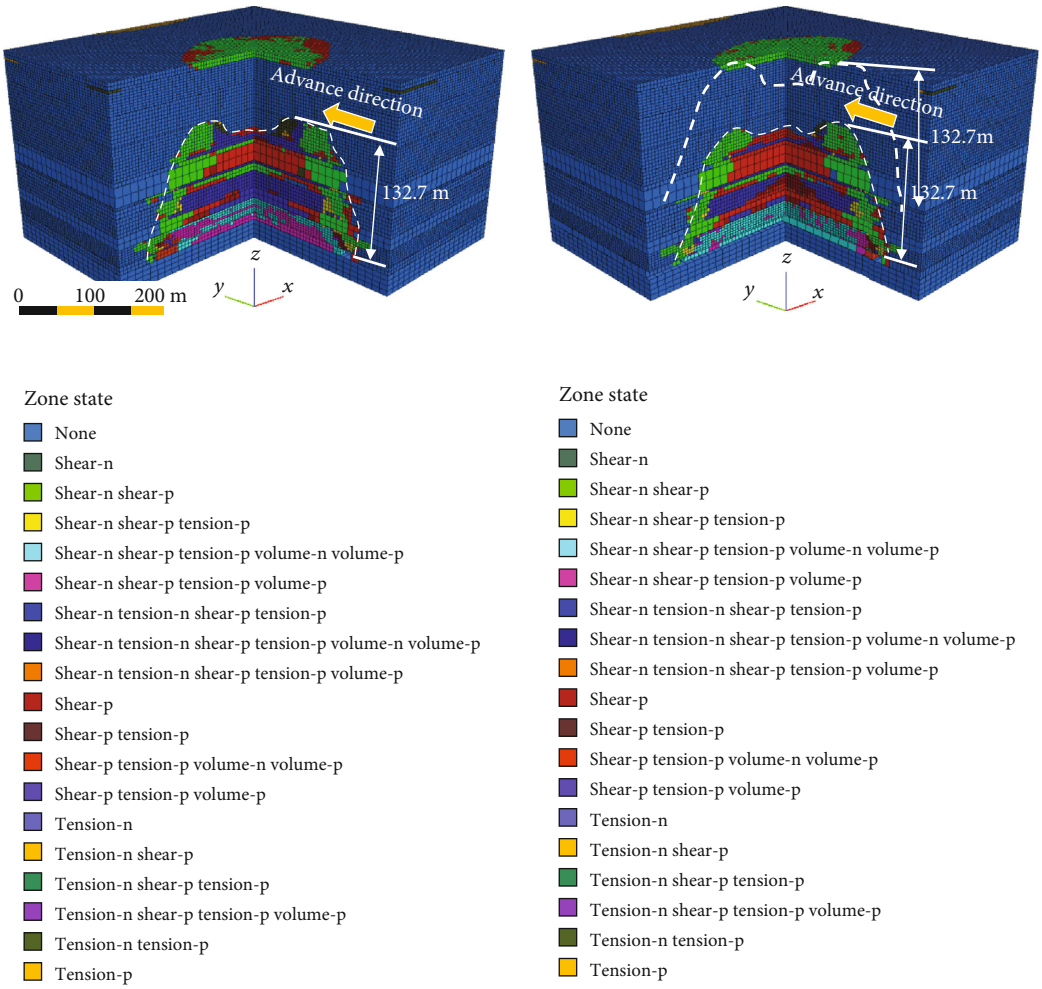

(a) 5 m/d (b) 13 m/d

Figure 9: Continued.

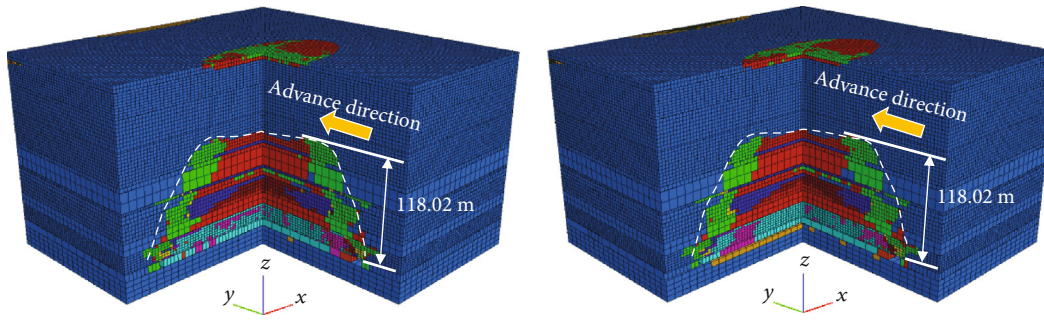

Zone state
- None
- Shear-n
- Shear-n shear-p
- Shear-n shear-p tension-p
- Shear-n shear-p tension-p volume-n volume-p
- Shear-n shear-p tension-p volume-p
- Shear-n tension-n shear-p tension-p
- Shear-n tension-n shear-p tension-p volume-n volume-p
- Shear-n tension-n shear-p tension-p volume-p
- Shear-p
- Shear-p tension-p
- Shear-p tension-p volume-n volume-p
- Shear-p tension-p volume-p
- Tension-n
- Tension-n shear-p
- Tension-n shear-p tension-p
- Tension-n shear-p tension-p volume-p
- Tension-n tension-p
- Tension-p

(c) 15 m/d

Zone state
- None
- Shear-n
- Shear-n shear-p
- Shear-n shear-p tension-p
- Shear-n shear-p tension-p volume-n volume-p
- Shear-n shear-p tension-p volume-p
- Shear-n tension-n shear-p tension-p
- Shear-n tension-n shear-p tension-p volume-n volume-p
- Shear-n tension-n shear-p tension-p volume-p
- Shear-p
- Shear-p tension-p
- Shear-p tension-p volume-n volume-p
- Shear-p tension-p volume-p
- Tension-n
- Tension-n shear-p
- Tension-n shear-p tension-p
- Tension-n shear-p tension-p volume-p
- Tension-n tension-p
- Tension-p

(d) 17 m/d

Figure 9: Continued.

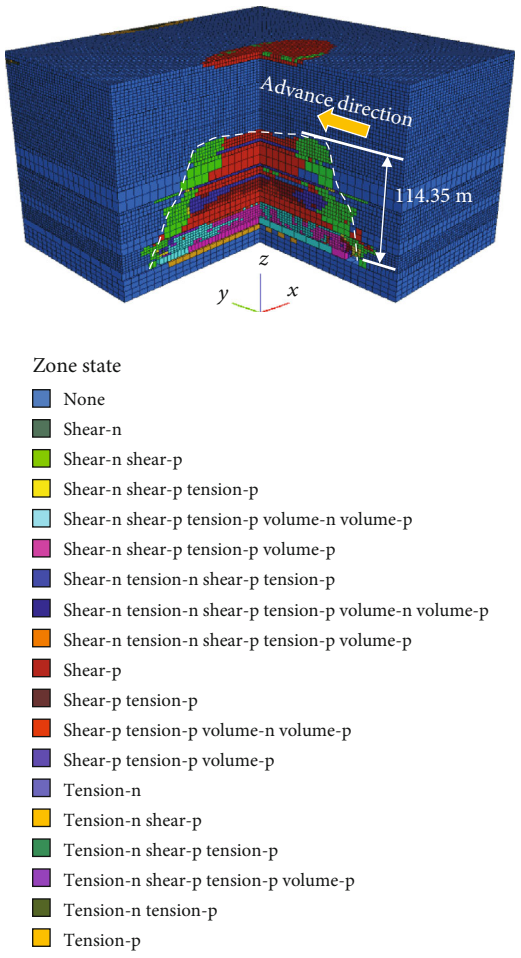

(e) 19 m/d

Figure 9: Distribution characteristics of plastic zones with different advancing speeds.

The sum of the mean value and standard deviation of the end-circulation resistance of supports was taken as the criterion to judge the first roof weighting (periodic roof weighting). The expressions are as follows:

$$\begin{cases} \bar{P}_i = \dfrac{1}{n}\sum_{i=1}^{n} P_{ti}, \\ \sigma_p = \sqrt{\dfrac{1}{n}\sum_{i=1}^{n}\left(P_{ti}\text{-}\overline{P_i}\right)^2}, \\ P_t = \overline{P_i} + \sigma_p, \end{cases} \tag{21}$$

where $\bar{P}_i$ is the mean value of the end-circulation resistance of supports, n is the number of monitoring cycles, P_{ti} is the end-circulation resistance of the support, σ_p is the standard deviation of the end-circulation resistance of the supports, and P_t is the first roof weighting (periodic roof weighting) criterion. Statistics for the end-circulation resistance of the supports were within 360 m of the advancing distance, and the results show that $\bar{P}_i$ =310.73 bar, σ_p =56.11 bar, and P_t =366.84 bar.

The distribution characteristics of the support working resistance of the panel 12401 are shown in Figure 12. In stage I, the first weighting interval was 38 m, and the periodic weighting happened 14 times with an average periodic weighting interval of 15.12 m. In stage II, the periodic weighting happened 6 times with an average periodic weighting interval of 18.33 m. As the acceleration of the advancing speed, the periodic weighting interval increased, which was consistent with the statistical results in Section 2. Compared with stage II, stage I has an uneven distribution of the working resistance and a more durable weighting, which was resulting in frequent crushing accidents.

Due to the cumulative effect of overburden damage, accelerating the advancing speed shortens the accumulation time of overburden damage, and the periodic weighting interval of the basic roof increases accordingly. Meanwhile, accelerating the advancing speed shortens the duration of the periodic weighting, which promotes rapidly forming stable structure for the basic roof, and the overburden damage reduces accordingly. Therefore, the reliability of numerical simulation results for the overburden damage degree is verified by the distribution characteristics of the support working resistance in two stages.

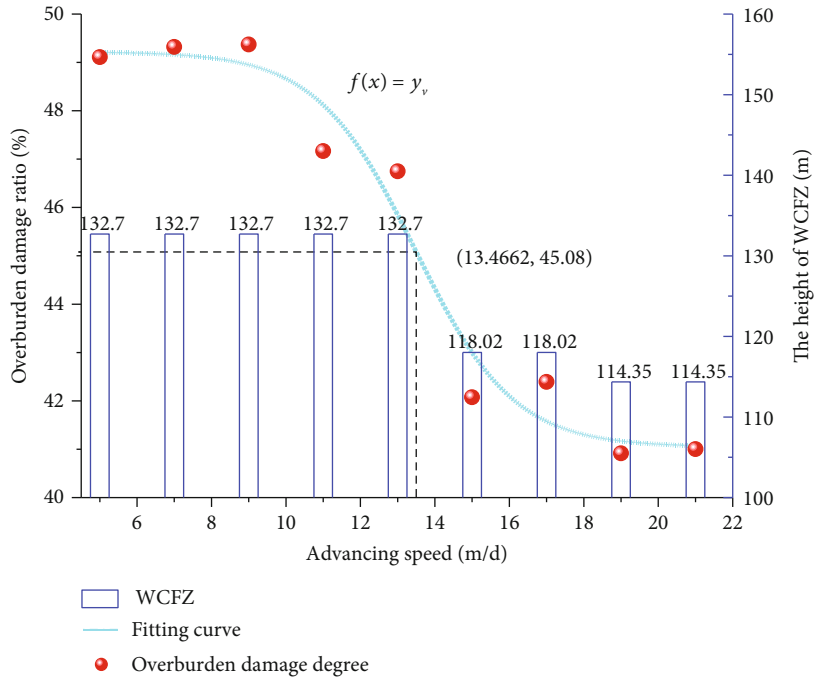

Figure 10: Overburden damage degree and the height of WCFZ versus advancing speed.

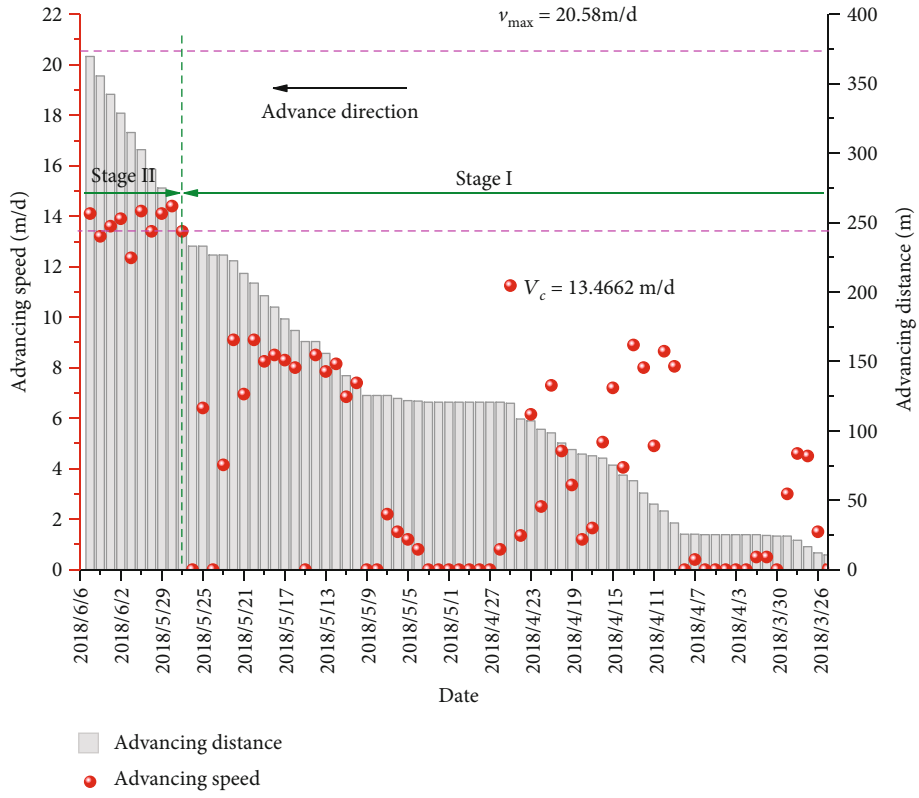

Figure 11: Statistics of the advancing speed and advancing distance of panel 12401.

6.2. Effects of Advancing Speed on Ground Cracks. Ground cracks are the external manifestation of the overburden damage caused by the high-intensity mining of the shallow coal seams. The surface of panel 12401 is a 0 to 27 m aeolian sand with weak shear and tensile resistance, which is prone to forming ground cracks [16]. As shown in Figure 13, dynamic ground cracks of the two stages in the middle of the panel 12401 were selected for comparison. In stage I, due to the

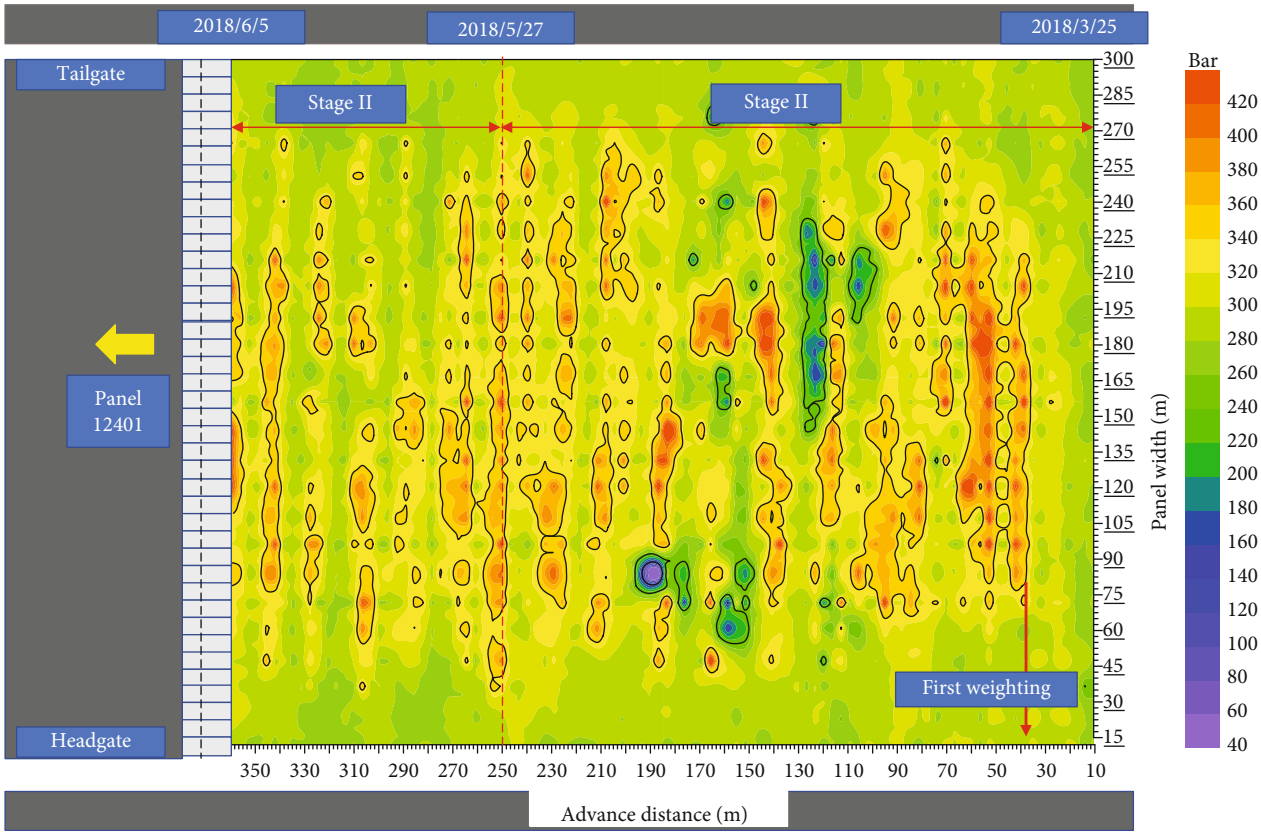

Figure 12: Distribution characteristics of the support working resistance of panel 12401.

(a) Tension ground cracks

(b) Stepped type ground cracks

Figure 13: Dynamic ground cracks in the middle of panel 12401.

low advancing speed, the overlying strata were in states of tension or shear for a long period, resulting in forming the stepped type ground cracks. In stage II, within a reasonable range of the advancing speed, the tension and shear time of the overlying strata is shortened. Thus, the surface failure is relatively weak, and only the tension cracks with small openings appear. The field engineering practice shows that the acceleration of the advancing speed weakens the damage degree of the overburden and surface. This conclusion is consistent with the numerical simulation results, which verifies the reliability of the numerical simulation and the validity of the overburden damage degree in describing overburden failure.

7. Discussion

The statistical analysis of the relationship between the mining parameters and periodic weighting interval in the western mining area was carried out, which indicated that mining

parameters have significant influence on overburden failure. The overburden damage degree index was defined to quantitatively characterize the damage degree of the mining-disturbed overburden in a three-dimensional space. The reasonable mining parameters of panel 12401 are 8.8 m in mining height, 300 m in panel width, and 13.47 to 20.58 m/d in advancing speed, which were determined by the FLAC3D simulation of the overburden damage degree. The measured results of the PWI and the ground cracks of the two stages verified the validity of the determination of the high-intensity mining parameters through the overburden damage degree method.

Previous studies on overburden failure mainly focused on the height and morphology of the WCFZ considering the profile of the overburden ([10–12, 22, 47]), while the overburden damage degree, defined in this study, is a variable in a three-dimensional space to describe the damage volume ratio of the overburden. Based on the relationship between the overburden damage degree and the mining parameters, the reasonable mining parameters can be obtained. In addition, the mining parameters are closely related to the PWI and the crack development. Therefore, the overburden damage degree promotes ground pressure control and the surface crack management.

The concept of the overburden damage degree proposed in this study has been effectively applied in the production practices of the Shangwan coal mine in China's western mining area. The validity of the overburden damage degree method will be further verified with different panel conditions in the future. The extraction of the overburden damage degree can be easily realized in the numerical models. However, methods for extracting the overburden damage degree from physical simulations and field engineering practices require a further study.

8. Conclusions

Taking the high-intensity mining working faces in the western mining area as the background, the effects of mining parameters on the PWI, the height of WCFZ, the damage degree, and the ground cracks were investigated in this study by employing a combined method of statistical analysis, FLAC3D numerical simulation, and field measurement. The reasonable range for mining parameters of the panel 12401 was provided based on the fitting function of the overburden damage degree versus mining parameters. The main conclusions are as follows:

(1) The PWI of the basic roof increases as the advancing speed increases, the mining height reduces, or the panel width shortens under constant engineering geological conditions. In other words, the degree of overburden damage degree will be weakened for one panel by increasing the advancing speed, reducing the mining height, or shortening the panel width

(2) The overburden damage degree quantitatively describes the overburden failure in a three-dimensional space, but the height and morphology of the WCFZ merely consider the profile of the overburden. The numerical simulation results show that the overburden damage degree is more accurate than the height of WCFZ in describing the overburden failure

(3) The variation range of the overburden damage degree influenced by the advancing speed and panel width is 41% to 49.37% and 19.98% to 88.02%, respectively, which means the overburden damage degree is more sensitive to the variation in panel width

(4) The reasonable mining parameters of the panel 12401 are 8.8 m in mining height, 300 m in panel width, and 13.47 to 20.58 m/d in advancing speed, respectively. The field measurement results of the PWI and ground cracks have verified the validity using the overburden damage degree to determine high-intensity mining parameters

Abbreviations

D: Damage variable
$\mathrm{d}V$: Volume of the unit body
$\mathrm{d}V_0$: Volume of the matrix
$\mathrm{d}V_D$: Volume of the damaged body
σ_{ij}: Rock mass stress
σ_{ij}^0: Matrix stress
J_2: Second invariants of the deviatoric stress tensor of the rock mass
J_2^0: Second invariants of the deviatoric stress tensor of the matrix
S_{ij}: Deviatoric stress tensor of the rock mass
σ_{mm}: Hydrostatic pressure
σ_{mm}^0: Hydrostatic pressure of the matrix
δ_{ij}: Kronecker symbol
E_{ijkl}: Elastic constant tensor of the matrix
ε_{kl}^0: Strain tensor of the matrix
ε_{kl}^D: Strain tensor of the damaged body
G: Shear modulus of the rock mass
G^0: Shear modulus of the matrix
$\bar{\sigma}$: Equivalent stress
$\bar{\varepsilon}$: Equivalent strain
h_f: Drillhole depth at the top of the WCFZ
W: Compression value of rock strata
M: Mining height
D_d: Overburden damage degree
V_i: Volume of a plastic zone
V_o: Observed space volume
$\bar{P}_i$: Mean value of the end-circulation resistance of supports
n: Number of monitoring cycles
P_{ti}: End-circulation resistance of the support
σ_p: Standard deviation of the end-circulation resistance of the supports
P_t: Threshold value of the roof weighting.

Data Availability

The data used to support the findings of this study are available from the corresponding author upon request.

Conflicts of Interest

The authors declared that they have no conflicts of interest to this work.

Acknowledgments

The financial support for this work was provided by the National Natural Science Foundation of China (Nos. 51874281, 51704274, and 51404272), the State Key Laboratory Cultivation Base for Gas Geology and Gas Control (Henan Polytechnic University) (WS2019A05), the Yue Qi Distinguished Scholar Project, China University of Mining & Technology, Beijing (2017JCB02), and the Fundamental Research Funds for the Central Universities (2020YQNY04).

References

[1] National Bureau of Statistics of China, *2018 national economic and social development statistical bulletin [EB/OL]*, 2018, http://www.stats.gov.cn/tjsj/zxfb/201902/t20190228_1651265.html.

[2] C. L. Wang, C. S. Zhang, X. D. Zhao, L. Liao, and S. L. Zhang, "Dynamic structural evolution of overlying strata during shallow coal seam longwall mining," *International Journal of Rock Mechanics and Mining Sciences*, vol. 103, pp. 20–32, 2018.

[3] W. B. Guo, G. B. Zhao, G. Lou, and S. Wang, "A new method of predicting the height of the fractured water-conducting zone due to high-intensity longwall coal mining in China," *Rock Mechanics and Rock Engineering*, vol. 52, no. 8, pp. 2789–2802, 2019.

[4] L. Sun, C. H. Li, Y. P. Cai, and X. Wang, "Interval optimization model considering terrestrial ecological impacts for water rights transfer from agriculture to industry in Ningxia, China," *Scientific Reports*, vol. 7, no. 1, p. 3465, 2017.

[5] X. Y. Liu, W. Zhou, and Z. K. Bai, "Vegetation coverage change and stability in large open-pit coal mine dumps in China during 1990–2015," *Ecological Engineering*, vol. 95, pp. 447–451, 2016.

[6] N. Li, C. Z. Yan, and J. L. Xie, "Remote sensing monitoring recent rapid increase of coal mining activity of an important energy base in northern China, a case study of Mu Us Sandy Land," *Resources, Conservation and Recycling*, vol. 94, pp. 129–135, 2015.

[7] Y. L. Bi, L. L. Xie, J. Wang, Y. X. Zhang, and K. Wang, "Impact of host plants, slope position and subsidence on arbuscular mycorrhizal fungal communities in the coal mining area of north-central China," *Journal of Arid Environments*, vol. 163, pp. 68–76, 2019.

[8] D. P. Adhikary and H. Guo, "Measurement of longwall mining induced strata permeability," *Geotechnical and Geological Engineering*, vol. 32, no. 3, pp. 617–626, 2014.

[9] Q. S. Bai and S. H. Tu, "A General Review on Longwall Mining-Induced Fractures in Near-Face Regions," *Geofluids*, vol. 2019, 22 pages, 2019.

[10] X. X. Miao, X. M. Cui, J. A. Wang, and J. L. Xu, "The height of fractured water-conducting zone in undermined rock strata," *Engineering Geology*, vol. 120, no. 1-4, pp. 32–39, 2011.

[11] V. Palchik, "Formation of fractured zones in overburden due to longwall mining," *Environmental Geology*, vol. 44, no. 1, pp. 28–38, 2003.

[12] A. Majdi, F. P. Hassani, and M. Y. Nasiri, "Prediction of the height of destressed zone above the mined panel roof in longwall coal mining," *International Journal of Coal Geology*, vol. 98, no. 1, pp. 62–72, 2012.

[13] Z. Y. Song, H. Konietzky, and M. Herbst, "Drawing mechanism of fractured top coal in longwall top coal caving," *International journal of rock mechanics and mining sciences*, vol. 130, article 104329, p. 130, 2020.

[14] J. X. Tang, Z. Y. Dai, Y. L. Wang, and L. Zhang, "Fracture Failure of Consequent Bedding Rock Slopes After Undergroundmining in Area," *Rock mechanics and rock engineering*, vol. 52, no. 8, pp. 2853–2870, 2019.

[15] C. Xu, Q. Fu, X. Y. Cui, K. Wang, Y. X. Zhao, and Y. B. Cai, "Apparent-Depth Effects of the Dynamic Failure of Thick Hard Rock Strata on the Underlying Coal Mass During Underground Mining," *Rock mechanics and rock engineering*, vol. 52, no. 5, pp. 1565–1576, 2019.

[16] X. L. Yang, G. C. Wen, L. C. Dai, H. T. Sun, and X. L. Li, "Ground Subsidence and Surface Cracks Evolution from Shallow-Buried Close-Distance Multi-seam Mining: A Case Study in Bulianta Coal Mine," *Rock mechanics and rock engineering*, vol. 52, no. 8, pp. 2835–2852, 2019.

[17] L. Q. Ma, Z. Y. Jin, J. M. Liang, H. Sun, D. S. Zhang, and P. Li, "Simulation of water resource loss in short-distance coal seams disturbed by repeated mining," *Environmental earth sciences*, vol. 74, no. 7, pp. 5653–5662, 2015.

[18] G. Wang, M. M. Wu, R. Wang, H. Xu, and X. Song, "Height of the mining-induced fractured zone above a coal face," *Engineering Geology*, vol. 216, pp. 140–152, 2017.

[19] J. C. Zhang, "Investigations of water inrushes from aquifers under coal seams," *International Journal of Rock Mechanics and Mining Sciences*, vol. 42, no. 3, pp. 350–360, 2005.

[20] C. Zhang, S. Tu, L. Zhang, Q. Bai, Y. Yuan, and F. Wang, "A methodology for determining the evolution law of gob permeability and its distributions in longwall coal mines," *Journal of Geophysics and Engineering*, vol. 13, no. 2, pp. 181–193, 2016.

[21] B. N. Hu, H. X. Zhang, and B. H. Shen, *Regulations of Coal Mining and Protective Coal Pillar Design under Buildings, Water Bodies, Railways, Coal Mines and Roadways*, Coal Industry Press, Beijing, Beijing, 2017.

[22] Y. Liu, Q. M. Liu, W. P. Li, T. Li, and J. H. He, "Height of water-conducting fractured zone in coal mining in the soil–rock composite structure overburdens," *Environmental Earth Sciences*, vol. 78, no. 7, p. 242, 2019.

[23] X. J. Hu, W. P. Li, D. T. Cao, and M. C. Liu, "Index of multiple factors and expected height of fully mechanized water flowing fractured zone," *Journal of China Coal Society*, vol. 37, no. 4, pp. 613–620, 2012.

[24] E. Jiránková, "Utilisation of surface subsidence measurements in assessing failures of rigid strata overlying extracted coal seams," *International Journal of Rock Mechanics and Mining Sciences*, vol. 53, pp. 111–119, 2012.

[25] J. F. Ju and J. L. Xu, "Structural characteristics of key strata and strata behaviour of a fully mechanized longwall face with 7.0m height chocks," *International Journal of Rock Mechanics and Mining Sciences*, vol. 58, pp. 46–54, 2013.

[26] Q. D. Qu, J. L. Xu, R. L. Wu, W. Qin, and G. Z. Hu, "Three-zone characterisation of coupled strata and gas behaviour in multi-seam mining," *International Journal of Rock Mechanics and Mining Sciences*, vol. 78, pp. 91–98, 2015.

[27] J. L. Xu, W. B. Zhu, and X. Z. Wang, "(2012). New method to predict the height of fractured water-conducting zone by location of key strata," *Journal of China Coal Society*, vol. 37, no. 5, pp. 762–769, 2012.

[28] Z. Y. Song, W. J. Wei, and J. W. Zhang, "Numerical investigation of effect of particle shape on isolated extracted zone (IEZ) in block caving," *Arabian Journal of Geosciences*, vol. 11, no. 12, p. 310, 2018.

[29] Z. B. Yu, S. Y. Zhu, Y. Z. Guan, and D. X. Hu, "Feasibility of Modifying Coal Pillars to Prevent Sand Flow Under a Thick Loose Layer of Sediment and Thin Bedrock," *Mine water and the environment*, vol. 38, no. 4, pp. 817–826, 2019.

[30] D. Y. Zhang, W. H. Sui, and J. W. Liu, "Overburden Failure Associated with Mining Coal Seams in Close Proximity in Ascending and Descending Sequences Under a Large Water Body," *Mine water and the environment*, vol. 37, no. 2, pp. 322–335, 2018.

[31] M. G. Qian, P. W. Shi, and J. L. Xu, *Ground pressure and strata control*, China University of Mining and technology Press, Xuzhou, 2010.

[32] H. F. Lin, R. F. Ma, S. G. Li, L. H. Cheng, H. Y. Pan, and L. Li, "Coupling model of evolution of mining fissure elliptic paraboloid zone and methane delivery," *Advanced Materials Research*, vol. 734-737, pp. 546–550, 2013.

[33] F. Wang, J. L. Xu, and J. L. Xie, "Effects of arch structure in unconsolidated layers on fracture and failure of overlying strata," *International Journal of Rock Mechanics and Mining Sciences*, vol. 114, pp. 141–152, 2019.

[34] C. Zhang, S. Tu, and Y. Zhao, "Compaction characteristics of the caving zone in a longwall goaf: a review," *Environmental Earth Sciences*, vol. 78, no. 1, pp. 27–46, 2019.

[35] L. Zhou, X. P. Su, Y. Y. Lu, Z. L. Ge, Z. Y. Zhang, and Z. H. Shen, "A New Three-Dimensional Numerical Model Based on the Equivalent Continuum Method to Simulate Hydraulic Fracture Propagation in an Underground Coal Mine," *Rock mechanics and rock engineering*, vol. 52, no. 8, pp. 2871–2887, 2019.

[36] M. Kachanov, "Effective properties of Solids: review of Concepts," *Applied Mechanics Reviews*, vol. 45, no. 8, pp. 304–335, 1992.

[37] S. Murakami, "Mechanical representation of damage and damage variables," in *Continuum Damage Mechanics: A Continuum Mechanics Approach to the Analysis of Damage and Fracture*, pp. 15–55, Springer Netherlands, Dordrecht, 2012.

[38] Z. Wang, L. Zhao, J. Kang, and L. Jia, "Technological study on height observation of water flowing fractured zone caused by repeated mining in multiple coal seam," *Coal engineering*, vol. 50, no. 12, pp. 82–85, 2018.

[39] Q. S. Bai, S. H. Tu, F. T. Wang, and C. Zhang, "Field and numerical investigations of gateroad system failure induced by hard roofs in a longwall top coal caving face," *International Journal of Coal Geology*, vol. 173, pp. 176–199, 2017.

[40] G. B. Zhang, W. Q. Zhang, C. H. Wang, G. L. Zhu, and B. Li, "Mining seams Bedrock–Deformation andfailure of strata and Alluvium," *Geotechnical and Geological Engineering*, vol. 34, no. 5, pp. 1553–1563, 2016.

[41] T. Zhang, Y. X. Zhao, Q. Gan, X. D. Nie, G. P. Zhu, and Y. Hu, "Investigations into Mining-Induced Stress–Fracture–Seepage Field Coupling in a Complex Hydrogeology Environment: A Case Study in the Bulianta Colliery," *Mine water and the environment*, vol. 38, no. 3, pp. 632–642, 2019.

[42] C. Zhang and L. Zhang, "Permeability Characteristics of Broken Coal and Rock Under Cyclic Loading and Unloading," *Natural Resources Research*, vol. 28, no. 3, pp. 1055–1069, 2019.

[43] Y. C. Luan, J. T. Li, X. H. Ban, C. Y. Sang, C. Q. Zhang, and D. P. Ma, "Observational research on the height of water flowing fractured zone in repeated mining of short-distance coal seams," *Journal of Mining and Safety Engineering*, vol. 27, no. 1, pp. 139–142, 2010.

[44] Y. Y. Lu, T. Gong, B. W. Xia, B. Yu, and F. Huang, "Target Stratum Determination of Surface Hydraulic Fracturing for Far-Field Hard Roof Control in Underground Extra-Thick Coal Extraction: A Case Study," *Rock mechanics and rock engineering*, vol. 52, no. 8, pp. 2725–2740, 2019.

[45] M. S. Yi, "Selection of echanzied working face length by great height mining under shallow coal seam in Shendong coal district," *Journal of China Coal Society*, vol. 2007, no. 12, pp. 1253–1257, 2007.

[46] J. H. Yang, S. L. Kong, and D. Z. Kong, "Effect of working face length and advancing speed on strata behaviors in high-intensity mining," *Rock and soil mechanics*, vol. S2, pp. 333–399+350, 2015.

[47] J. A. Wang and H. D. Park, "Coal mining above a confined aquifer," *International Journal of Rock Mechanics and Mining Sciences*, vol. 40, no. 4, pp. 537–551, 2003.